

THE PENNSYLVANIA STATE UNIVERSITY
SCHREYER HONORS COLLEGE

DEPARTMENT OF ASTRONOMY & ASTROPHYSICS

SOFT X-RAY SOURCE MODELING OF THE CYGNUS LOOP & PREDICTED
OBSERVATION FOR THE ROCKET FOR EXTENDED-SOURCE X-RAY SPECTROSCOPY

VINCENT A. SMEDILE
Spring 2023

A thesis
submitted in partial fulfillment
of the requirements
for a baccalaureate degree
in Astronomy & Astrophysics
with honors in Area of Honors

Reviewed and approved* by the following:

James H. Tutt, PhD
Associate Research Professor of Astronomy & Astrophysics
Thesis Supervisor

Alexander Wolszczan, PhD
Evan Pugh Professor of Astronomy & Astrophysics
Honors Adviser

*Signatures are on file in the Schreyer Honors College.

Abstract

Historically, the Cygnus Loop has been observed in multiple pointings and either large field of view soft X-ray instruments with poor resolution or highly resolved instruments that boast only moderate fields of view $\text{FOV} \leq 1^\circ \times 1^\circ$. I present both a source model for the Cygnus Loop Supernova Remnant (Cygnus Loop SNR) and the potential spectra recorded by the Rocket for Extended-source X-Ray Spectroscopy (tREXS), which is a sounding rocket with experimental optics created at Penn State. Given the expected timescales for the SNR. The source model is a two-temperature Non-equilibrium Ionization model. The model presented has a $\chi^2_\nu \sim 1.502$. Despite an attempt to fit a Non-equilibrium Ionization and Collisional Ionization Equilibrium model, the two-temperature Non-equilibrium Ionization model proved to fit best. The spectra used for this model were taken from a single 3° diameter pointing by HaloSat using the SDD38 and SDD54 detectors. The resulting source model was then treated as a source spectra and run through a ray-tracing instrument simulation model of tREXS to determine what the tREXS optic would observe in the field. The instrument model yielded a high-resolution spectrum, particularly around the lower wavelengths, with strong predicted transition lines at O VII, O VIII, N VII, and C VI. The model predicts a high-intensity ratio between O VII and O VIII, as well as depletions for C, N, and O abundances. Cygnus Loop currently has yet to have a soft X-Ray observation that encompasses the full width of the SNR with a single pointing. These models provide new insight into what a full 3° diameter field of view observation of Cygnus Loop SNR with tREXS is and bolster predictions for the spectral observations made by the novel passive focuser optic the rocket employs.

Table of Contents

List of Figures	iii
List of Tables	iv
Acknowledgements	v
1 Introduction	1
1.1 Overview of Supernova Remnants and Expansion	2
1.2 The Cygnus Loop Supernova Remnant	3
1.3 Limitations on Cygnus Loop Observations	6
1.4 The Rocket for Extended-source X-Ray Spectroscopy	7
1.5 HaloSat Observation of Cygnus	9
2 Modeling of the Source Spectra: Methods & Results	10
2.1 The Uchida Model	11
2.2 The HaloSat Source Model	13
3 The tREXS Instrument Model & Predicted Observation	17
3.1 The Instrument Model	18
3.2 Prediction for the Observed Spectra of Cygnus Using tREXS	21
4 Discussion of Results & Concluding Remarks	24
4.1 Discussion	25
4.2 Conclusion and Future Work	26
References	27
Academic Vitae	30

List of Figures

1.1	X-Ray Map of Cygnus Loop	3
2.1	Uchida Observations of Cygnus Loop	11
2.2	Uchida Sub-Regions of Cygnus Loop	12
2.3	Chi Square per Energy for the HaloSat source model	14
2.4	HaloSat source model Fit	16
3.1	Mechanical Beam Shaper Simulation	18
3.2	Spectral Gratings Simulation	20
3.3	Uchida-Based tREXS Predicted Observation	21
3.4	tREXS Predicted Observation by Miles (2021)	22

List of Tables

2.1	Uchida Source Model Parameters	13
2.2	HaloSat Source Model Parameters	15

Acknowledgements

To God, the knower and maker of all things, the mind all physicists seek to know, and the one who gave me the ability to comprehend and understand this vast and beautiful universe.

To my parents, family, and cherished loved ones for being my light, my life, my inspiration, and for continually pushing me to exceed my limitations. Because of all of you, a kid from Queens was able to go from a solar system book in a Long Island bookstore to an Astrophysics degree.

To my partner, who pushes me to exceed myself, to have confidence in my abilities, and helps to make me a better man single every day.

To my friends, who filled my life with joy when there was none and supported me throughout my undergraduate career to survive and thrive.

To my professors and teachers, who engaged me, kept my fire for science alive, and instilled in me a love of knowledge, research, and learning.

To the late Professor Hawking, whose book, *A Brief History of Time*, inspired me to become an astrophysicist and irrevocably changed my life.

"If we do discover a Theory of Everything...it would be the ultimate triumph of human reason—for then we would truly know the mind of God."

— *Prof. Stephen Hawking, A Brief History of Time*

Chapter 1

Introduction

1.1 Overview of Supernova Remnants and Expansion

Supernovae (SNs) are often some of the most striking visuals in the night sky. When they occur, SNs become some of the most luminous objects in the night sky and can even outshine galaxies in some cases. SNs are massive explosions generated by collapsing aged stars of a certain mass. However, what SNs leave behind produces far more long-lived emissions and phenomena than the initial explosion. The end product of an SN is a Supernova Remnant. Supernova Remnants (SNRs) are the results of the interaction between the ejecta and radiation produced by SNs and the surrounding Interstellar Medium (ISM). Many of the most known SNRs are characterized by a shell of ejecta surrounding a cavity and/or a compact object center.

After a SN occurs, SNs undergo a period of free expansion, characterized by the ejecta and emissions from the SN event itself freely passing through the vacuum of space (Chevalier, 1977; Spitzer, 1998). Due to the violent nature of most SN events, an SNR will often feature a cavity in the ISM or surrounding material generated by the force of the SN event, although in some cases these can occur naturally (Chevalier, 1977; Spitzer, 1998; Ciotti and D’Ercole, 1989; McEntaffer and Brantseg, 2011).

As the SNR expands, the primarily kinetic energy is transferred from the ejecta to the surrounding medium. The ejecta begins to sweep up material from the surroundings and begins to resemble a piston expanding and acting upon a gas. Eventually, the pressure from the ejecta pushing into the ISM creates a shockwave that drives itself into the ejecta, followed by a reverse shock. The reverse shock causes the start of the deceleration of the ejecta, and together with the main shock heats the ejecta and causes the development of clusters of ejecta. The clusters and knots of ejecta develop due to the pressure differences created within the ejecta by the reverse shock and the gas density varying between the point of contact with the ISM and ejecta further from this site (Chevalier, 1977; Spitzer, 1998).

As the shocked material loses kinetic energy and the shockwave from the ISM-ejecta collision weakens, the radiative emissions from the shock-heated gas cause it to cool behind the shockwave. The shock heats the ejecta to a high enough temperature that X-Ray emissions are common as the ejecta begin their long cooling timescale. It should be noted that gases in this stage begin in a non-equilibrium ionization (NEI), but slowly reach a collisional ionization equilibrium (CIE) over time (Chevalier, 1977; Spitzer, 1998). These models are generally utilized depending on the theorized stage of the evolution of SNR plasma. CIE models represent a phase of Ionization Equilibrium or a plasma that is optically thin, low-density, and in a quasi-steady state or steady state of some kind. Thus, in CIE the ionization balance of the plasma is treated as time-independent and solely reliant on particle collisions (Bryans et al., 2006). As a result, scholarship tends to use CIE models for SNRs in Sedov-Taylor or Radiative phases. NEI models represent Non-Equilibrium ionization, or plasma emissions are the result of a sudden change in a system in ionization equilibrium, such as a plasma that has just been shocked and superheated (Prokhorov, 2010). This makes them more applicable to SNRs that have just recently come into contact with the ISM or have swept up enough surrounding media to begin experiencing the shock and reverse shock.

In some cases, an SNR can form within a preexisting cavity. This is known as a Cavity Explosion SNR, which can prove a challenge when observing the SNR’s soft X-Ray emissions (Ciotti and D’Ercole, 1989). Cavity Explosion SNRs undergo expansion through a hot and dilute gas surrounded by a colder shell made from dense ISM material. The cavity is formed by the pro-

genitor star's stellar wind pushing away the surrounding media until it produces enough pressure to halt the expansion. During this stage, the shock of the stellar wind encounters a reverse shock from the dense displaced media, resulting in a heated media. Eventually, this cavity wall cools and condenses, while the remaining surrounding gases remain hot. This results in a cool dense shell and a largely vacant and hotter interior that the SNR must evolve through. This allows the SNR to freely expand without sweeping up much material from the media until it encounters the ISM barrier, rather than the traditional expansion denoted previously (Ciotti and D'Ercole, 1989). This expansion method still can result in Chevalier (1977)'s solutions to the evolution of an SNR as well (Ciotti and D'Ercole, 1989; Chevalier, 1977). However, because of the already dense cavity walls, Soft X-Ray observations of a cavity explosion SNR may not always be possible. Thus, examples of close and low extinction cavity explosion SNR such as the Cygnus Loop provide valuable theoretical insight into the expansion of SNRs under these conditions (Ciotti and D'Ercole, 1989; Fesen et al., 1982; Blair et al., 2005).

1.2 The Cygnus Loop Supernova Remnant

The Cygnus Loop Supernova Remnant is frequently studied for its close proximity of 540 pc (Blair et al., 2005), low extinction (Fesen et al., 1982), and large angular diameter of $\sim 3^\circ$ (Levenson et al., 1997). Cygnus Loop SNR is middle-aged (~ 10000 yr) and appears to have evolved in a preexisting cavity, making it a cavity explosion SNR. This age indicates that Cygnus Loop SNR features shocked ejecta and surrounding ISM and a still-expanding blast wave (Tsunemi et al., 2007). The average column density along the line-of-sight to the Cygnus Loop is $N_H \sim 3.14 \times 10^{20} \text{ cm}^{-2}$ (Uchida et al., 2009b).

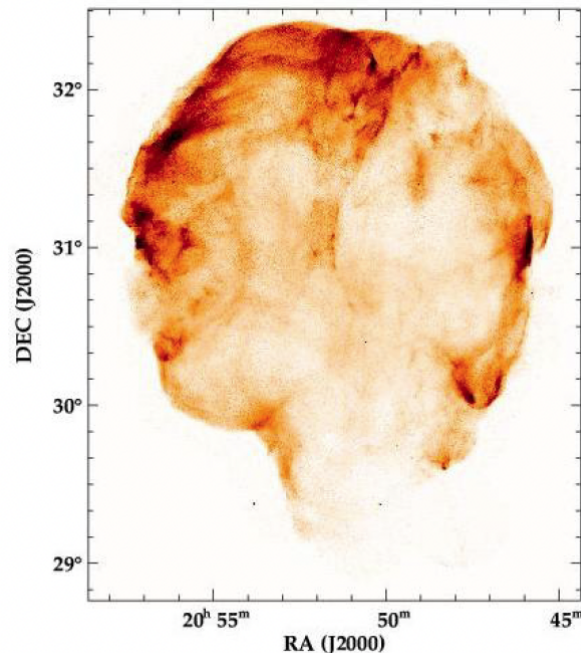


Figure 1.1: The view of the Cygnus Loop SNR as seen by *ROSAT* in Levenson et al. (1999).

Levenson et al. (1998) found that the evolution of the blast wave was found to be inconsistent with blast wave propagating through a uniform medium, nor is it consistent with a radiative or Sedov-Taylor expansion (Sedov, 1993; Levenson et al., 1998, 1999). As a result, its expansion and development will be governed by the denser-than-average ISM, which has been compacted due to the progenitor star stellar winds (Levenson et al., 1998). The preexisting cavity has caused the SNR to expand through a diffuse, lumpy, and nonuniform media, with the ejecta hitting the higher density of the ISM only within the last ~ 1000 yr (Hester et al., 1994). This relatively recent encounter with the ISM means that the blast wave has not yet hit the denser parts of the cavity wall (Hester et al., 1994; Levenson et al., 1998). Thus Cygnus Loop has not experienced the traditional expansion process during which the SNR blast wave and not the progenitor star sweeps up the ISM. This presents a unique opportunity to study the expansion of an SNR which has undergone non-uniform expansion and not encountered the ISM until relatively recently on a cosmic timescale (Ciotti and D’Ercole, 1989; Levenson et al., 1998; McEntaffer and Brantseg, 2011).

Soft X-Ray study of Cygnus’ emissions began in 1970 with Grader et al. and were continued by Gorenstein et al. (Grader et al., 1970; Gorenstein et al., 1971). These observations confirmed that Cygnus was $\approx 3^\circ$ in diameter and that the structure was of an x-ray emitting shell-like structure surrounding the optical filaments with little emission toward the center (Gorenstein et al., 1971). Varying observations and models have produced different results for the Cygnus Loop temperature, with competing models for non-equilibrium and equilibrium ionization. Some favor NEI, while others favor CIE or a combination of both (Levenson et al., 1999; McEntaffer and Brantseg, 2011; Miyata et al., 2007; Uchida et al., 2009b,a). Two temperature models are generally favored but some have utilized a single temperature model as well (Uchida et al., 2008, 2009b; Miles, 2021).

Vedder et al. (1986) took some of the highest resolution spectra of Cygnus Loop SNR to date, and found evidence for both CIE and NEI models. Vedder et al. used the Einstein Observatory Focal Plane Crystal Spectrometer to observe the O VII and Ne IX lines coming from the SNR. Vedder et al. were able to fit a single-temperature nonequilibrium plasma model with temperature $\sim .26$ keV despite initially theorizing a CIE fit due to a lack of forbidden line emission observations in the O VII trio. Despite this, surface brightness and detected lines are more consistent with equilibrium plasma emission of solar abundance and a temperature of $\sim .26$ keV. The best fit model found that the collisional timescale was between $10^{10} - 10^{11} \text{ cm}^{-3} \text{ s}$ (Vedder et al., 1986).

Cygnus has been studied on a larger scale by *ROSAT* (Levenson et al., 1997, 1999), in tiles across the SNR with *Chandra* (Levenson et al., 2002; Uchida et al., 2008), and in small-scale regional high resolution with *Suzaku* and *XMM-Newton* (Miyata et al., 2007; Tsunemi et al., 2007; Zhou et al., 2010; McEntaffer and Brantseg, 2011). Each has produced studies detailing varying best-fit models. A prolific and expansive study of Cygnus was done by Levenson et al. (1997), which performed a 24-pointing analysis of Cygnus using *ROSAT*’s Position Sensitive Proportional Counter (FWHM $\sim 10''$ resolution). It was found that the x-ray emissions are brightest along the interior of the circle that circumscribes the cavity. Using Sedov’s calculations it was concluded that the remnant is not a Sedov remnant. The high spatial-resolution and multi-pointing view of the Cygnus loop reveals a near-circular shape with interactions with large-scale inhomogeneities in the ISM. Furthermore, Levenson et al. (1997) found that neither NEI nor CIE models provide an adequate fit and found that a two-temperature CIE model fit more globally while a two-temperature NEI model fit better in certain regions. Admittedly these uncertainties could be due to limitations on *ROSAT*’s resolution. The SNR was modeled as having low ($\sim .06$ keV) and high temperature

($\sim 0.25\text{keV}$) regions. The observations do indicate that there is a global deceleration in the Cygnus Loop blast wave within the cavity walls (Levenson et al., 1997, 1998).

Miyata et al. (2007) used *Suzaku* to observe the NE limb region of the Cygnus loop and confirmed the observation of the OVIII lines previously detected by Vedder et al. (1986). There was also clear evidence of the first recorded C VI and N VI emissions from Cygnus. Miyata et al. (2007) applied and fit a single temperature NEI model but found it inadequate. A two-temperature NEI model was able to achieve an adequate best fit. The temperatures for the model decrease as the radius outward increases and were $\sim 0.10\text{keV}$ for the lower temperature and $\sim 0.25\text{keV}$ for the upper temperature. Miyata et al. (2007) were able to determine abundances for C, N, O, Ne, Mg, Si, and Fe for the first time and found their abundances to be depleted, but could not determine an abundance for He. They also found that the abundance of the X-ray emissions was confirmed to be where the ISM and blast wave are coming into contact (Miyata et al., 2007). As a result of this, Miyata et al. (2007) suspects that there are multiple phases of evolution occurring within the shell region and cited insensitivity in resolution as a reason for a lack of discussion on a global view of Cygnus.

Uchida et al. (2009a) performed an analysis of the ejecta using *Suzaku* and *XMM-Newton* pointings. 14 pointings were taken from *Suzaku* and 7 were taken from *XMM-Newton*. By combining tiled observations, they were able to span the diameter of Cygnus Loop and calculate the heavy element abundances via emission lines. The model employed was a two-temperature NEI model, with the lower temperature components being $kT \sim 0.28\text{keV}$ and the higher being $kT \sim 0.60\text{keV}$. They found metal deficiencies, particularly in oxygen ($\sim 0.10\odot$), than those presented in past studies such as Miyata et al. (2007). Lastly, the authors found a “metal circle”, or a region of more pronounced metal abundances within the more interior high- kT component, and discovered that the metal abundances there were non-uniform (Uchida et al., 2008, 2009a). This study was done in tandem with Uchida et al. (2009b), of the shell structure of Cygnus in 2009. Using 41 pointings from *Suzaku* and *XMM-Newton*, Uchida et al. (2009b) were able to once again fit a two-temperature component NEI model. Uchida et al. (2009b) again confirmed that the higher temperature and low-temperature components of the SNR originate from the exterior ejecta and ISM interacting and the reverse-shock heated interior ejecta. In doing so, they found an average temperature of $kT \sim 0.23\text{keV}$ and $kT \sim 0.52\text{keV}$ for the lower and higher temperature components, respectively. The recorded emission measures for the ISM indicate a nonuniform cavity wall, as discussed by McEntaffer & Brantseg in 2011 (Uchida et al., 2009b; McEntaffer and Brantseg, 2011).

Tsunemi et al. (2007) performed a study of the Southwestern Rim using *XMM-Newton* data. Their results indicated that the rim regions can be fit by a single-temperature component NEI model whereas the inner region requires a two-temperature component NEI model. They conclude that the low kT is $\sim 0.2\text{keV}$ and a high kT of $\sim 0.6\text{keV}$. The high-temperature region had higher abundances for metals and was recorded to be $\sim 5\odot$. Lastly, their results indicate that the cavity wall flux displays non-uniformity and that O, Ne, and Mg are more abundant in the outer region whereas Si, S, and Fe were more concentrated toward the inner region. The larger abundance of heavier elements in the inner region is thought to be tied to the progenitor star (Tsunemi et al., 2007). Zhou et al. (2010) found with *XMM-Newton* data that the low-temperature interior be $kT \sim 0.07 - 0.15\text{keV}$ and the higher-temperature exterior to be $kT \sim 0.24 - 0.46\text{keV}$ (Zhou et al., 2010). Uchida in 2008 performed a spectral fitting of the southwestern region known as the “blowout region.” The observations were taken using two *XMM-Newton* pointings (Uchida et al., 2008). They fit a two-temperature NEI model and recorded temperatures of $kT \sim 0.2\text{keV}$ and

$kT \sim 0.40\text{keV}$ for the lower and higher temperature regions, respectively. Despite the overall model fitting these temperatures globally, regional inconsistencies were found to exist, with some areas varying by $kT \pm 0.1 - 0.2\text{keV}$ (Uchida et al., 2008).

More recently, using *Chandra* data Oakley et al. (2013) found that temperature varies inversely with the densities of the regions along the cavity wall, with low-temperature components an order of magnitude higher in density than higher-temperature sections. The higher-density plasma exists nearer the cavity wall where it equilibrates and cools radiatively, whereas the lower-density plasma is more interior and is heated further by shock heating. In general, the lower temperature region is $\sim 0.11\text{keV}$, and the higher is $\sim 0.27\text{keV}$. These regions were approximated best by a two-temperature equilibrium (CIE) model. All regions displayed consistent metal depletions most notably in N, O, and Ne at an average of 0.54, 0.55, and 0.36 solar abundance, respectively. Given the timescales and shock velocities calculated, they concluded that the precursor wind that blew the cavity was $\sim 14\text{pc}$ in radius and that the time since interaction with the reverse shock has been long enough for the plasmas to equilibrate (Oakley et al., 2013). Concludes that the lack of broadband spectra and large FOV high-resolution images are poor and are necessary to validate spectral models of the source.

1.3 Limitations on Cygnus Loop Observations

Given the results of the previous section, it is clear that there are many discrepancies when comparing Cygnus Loop observations. Oakley et al. (2013) raise that several sources with different instruments at different times may cause systemic uncertainties and inadequate precision. As we have seen, this translates to such studies being somewhat representative, but due to the systemic uncertainties likely lack consistency with one another. They cite the various discrepancies in models and regional differences that arise when such studies are undertaken. Thus, Oakley et al. (2013) find that the integrated spectrum of the entire Cygnus Loop would validate these regional spectral studies, help discern the overall combination of CIE vs NEI plasma models and components, resolve discrepancies over the average temperatures of the interior ejecta and along the region where the blast wave interacts with the ISM Oakley et al., 2013.

Oakley et al. (2013) also raise the technology issue with observations of Cygnus. Due to the extended emission of the SNR, the previous studies were unable to use dispersive spectroscopy and were thus limited in the achievable spectral resolution. Thus, resolving power was sacrificed for extended FOV for many of these studies such as Levenson, Tsunemi, and Uchida (Levenson et al., 1999; Tsunemi et al., 2007; Uchida et al., 2008). In contrast, previous extended-source observations of the entire Cygnus Loop Gronenschild (1980) utilized proportional counters with an energy resolution of several hundred eV, but lacked the spectral resolution necessary for detailed modeling of the source.

Miles (2021) added onto the work from Oakley et al. (2013), and cites the need for an instrument that can resolve the separate ion species or is sensitive enough to the continuum emission. These are vital to properly diagnosing and modeling the plasma phenomena within the Cygnus Loop's soft X-ray emitting areas. Moreover, an instrument that can resolve the individual components of the He-like O-VII triplet and the other dominant emission lines are significantly increase what we know about Cygnus (Miles, 2021). This would require an $R \approx 110$ spectral resolution to differentiate between the intercombination transitions at $\approx 568.6\text{eV}$ and the resonance transi-

tion at $\approx 574eV$ (Miles, 2021). Modern X-Ray diffraction gratings, including older ones such as the ones on observatories like *Chandra* and *XMM-Newton*, have the necessary resolving power to resolve the O-VII triplet. In many cases, even ones with relatively poor performance can exceed the requirements needed to resolve an O-VII triplet. Thus, pairing a grating spectrometer with an optic capable of providing a wide enough FOV would have the requirements necessary to analyze the full Cygnus Loop spectra at once (Miles, 2021).

Based on this and the previous section’s discussion of Cygnus Loop observations, it is clear that there is a lack of global studies encompassing Cygnus’ entire 3° diameter and a lack of agreement on the abundances and plasma model at a global scale. Models either must utilize multi-pointing observations to sufficiently resolve the spectral features at a scale that is capable of covering Cygnus’ wide diameter or take multiple pointings of a small region of the SNR and assume that the region is representative of the whole. Despite this, both kinds of efforts have led to varying calculations for the abundances and plasma conditions for the remnant. The usage of smaller regions and pointings is useful for uncovering localized inhomogeneities and region-specific models and conditions but does not give a clear representation of the whole. Generally, most studies tend to agree on two-temperature models and agree that there are low and high-temperature regions that are somewhere between $\sim 0.1keV \leq kT \leq 0.3keV$ and $\sim 0.3keV \leq kT \leq 0.6keV$, respectively. These models also vary in their interpretations of abundances, with some recording higher abundances of metals and others reporting deficiencies with past models. For example, Tsunemi et al. (2007) reported higher O abundances than Uchida et al. (2008) reported.

It is clear then, that a single pointing $\sim 3^\circ \times 3^\circ$ field of view (FOV) observation with an adequate resolution to resolve spectra features such as the O-VII triplet and forbidden lines is key to determining a model that is holistically representative of Cygnus. To achieve this, an instrument with both a $\sim 3^\circ \times 3^\circ$ FOV and a resolving power of $R \approx 110$ is necessary. Should this be possible, it opens the possibility for higher-resolution spectra and emission lines of interest from other sources such as other SNRs, and the X-Ray Background itself. The Rockets for Extended-source X-Ray Spectroscopy carry both an optic capable of achieving the necessary FOV and grating spectrometers capable of resolving the necessary emission lines.

1.4 The Rocket for Extended-source X-Ray Spectroscopy

The Rockets for Extended-source X-Ray Spectroscopy are a series of NASA-funded sounding rocket missions led by the Pennsylvania State University (PSU) (Miles et al., 2019; Tutt et al., 2021; Miles, 2021). The tREXS payload achieves the desired science goals of observing a diffuse soft X-ray source like Cygnus Loop through a combination of novel passive mechanical focusing optics, custom diffraction gratings, and CIS113 CMOS detectors capable of imaging the entire diffracted spectrum while maintaining a signal-to-noise (S/N) sufficient enough to detect each X-ray event. This design is meant to apply and transferable to different spacecraft formats, such as CubeSats, sounding rockets, and larger orbital observatories (Miles et al., 2019).

tREXS is equipped with optics designed to provide the sufficiently large FOV needed to fully observe diffuse sources. The tREXS grating spectrometer achieves resolving power by spatially dispersing the optics point spread function via grating diffraction. However, because the resolving power is dependent on only one dimension, the necessary resolution can be achieved by a 1D focusing optic that allows for the same resolution as a 2D system can. As such, tREXS utilizes a

1D mechanical beam shaper (MBS) to focus the incident photons into a 1D point spread function, also called a line spread function (LSF), that achieves the desired resolution from the X-ray gratings (Miles et al., 2019; Tutt et al., 2019; Miles, 2021).

An MBS is a method of passive focusing that is generally comprised of a series of collimators. These collimators manipulate the incoming light by only allowing photons whose incident angles fall within a certain distribution to pass through the optic and interact with other components of the payload. tREXS utilizes a custom MBS to replicate the ability of reflective optics. The tREXS MBS consists of a series of plates that feature several aperture slits arrayed perpendicular to the optical axis. The number of slits per plate is conserved, but the slit positions and apertures converge along the optical axis to allow photons that fall within the acceptable range of incident angles and occult ones that do not. Because of the constant number of slits per plate, the plates when overlapped with one another combine to form the desired LSF. The exterior-most slits in each plate have a larger convergence angle than the interior slits to ensure all individual slit paths come to the same focus and desired focal length. The MBS also provides a modular aspect that allows for a change in FOV and collection area by manipulating the number of slits or the sizes of the slit convergence angles. When designing the tREXS optics, different optics were considered, including a 1D Lobster-eye optic and a 1D Kirkpatrick-Baez optic. Despite this, a single channel of passive MBS provided an order of magnitude higher effective area. Moreover, the tREXS MBS is designed to be a standalone optic with a single channel, meaning that an instrument can host one or many MBS channels and increase the sensitivity with each added channel. The current design of tREXS features four MBS, while the most recent launch only included two. The presence of multiple channels means that tREXS actually exceeds the required FOV and collection area necessary to fully observe Cygnus Loop (Miles et al., 2019; Tutt et al., 2019; Miles, 2021).

While achieving the best possible FOV and collection area, tREXS still requires spectral diffraction gratings capable of achieving the maximum possible resolution. The goal is to ideally detect the emission lines needed to characterize the plasma, namely CVI, OVII, and OVIII (Miles et al., 2019). However, due to the short exposure time (≈ 300 s) amount of counts is expected to be slim (Miles et al., 2019; Miles, 2021). Thus, the chance to capture the O VII intercombination transition is very low, and as such, the resolution was scaled to $R \approx 60$ to boost the count rate at the expense of only viewing two of the three O VII triplet lines. The gratings must also preserve the focus created by the MBS modules, which is dependent on the fabrication quality, grating dispersion, and the physical scale of the instrument (Oakley et al., 2013; Miles, 2021). The master spectral gratings were produced at PSU using a Littrow configuration and were reproduced using SCIL replication (Miles, 2021). The design settled on a groove spacing of $150 \lesssim d \lesssim 200$ nm and a facet angle of $\approx 30 - 40^\circ$. After fabrication, the grating measurements came out to a facet angle of $\delta = 32^\circ$ and a groove spacing of 181.0 nm. These dimensions ensure that the wavelengths are diffracted preferentially to be detected properly by the detectors (Miles, 2021).

In short, the flow of X-ray photons through the instrument would be as follows. Once the rocket is pointed at the center of the Cygnus Loop SNR, the photons enter through the aperture and into the MBS. The MBS is designed to occult all other photons that pass through at incident angles that don't match photons from Cygnus Loop SNR. The MBS will shape the photons into the LSF, which then pass through the spectral gratings to be separated by wavelength. Lastly, the CIS113 CMOS detectors record the spectra.

The first tREXS launch observed Cygnus Loop and was launched from White Sands Missile Range, New Mexico USA in September 2022. The attempt to gain soft X-ray photons from Cygnus

was a failure, however, as a malfunction exposed the detectors to water vapor which condensed onto the detectors and absorbed any potential photons from the source. Due to a lack of real data, building an instrument model that can take a source model and return expected observation parameters is vital to the development of the tREXS missions. A proper source model can only be built from a dataset that has a full $3^\circ \times 3^\circ$ FOV of Cygnus Loop. The recent HaloSat data, despite having poorer resolution than tREXS, provides this and thus is an adequate substitute for the source (Kaaret et al., 2019; Miles, 2021).

1.5 HaloSat Observation of Cygnus

HaloSat is the first astrophysical CubeSat mission funded by NASA’s Science Mission Directorate (Kaaret et al., 2019). The mission’s expressed purpose is to estimate the mass of the hot halo surrounding the Milky Way, and as such is designed to measure elemental abundances and resolve soft X-ray oxygen emissions at 10^6 Kelvin (Kaaret et al., 2019). At 10^6 kelvin, oxygen produces strong emissions of lines near 574eV, which result in the O VII triplet and O VIII doublet that past observations of Cygnus have sought (Vedder et al., 1986; Levenson et al., 1997; Uchida et al., 2009a; Oakley et al., 2013; Kaaret et al., 2019). To image the spectra, HaloSat features three independent detector instruments that utilize Silicon Drift Detectors (SDDs) to detect X-rays. Each detector also boasts a multilayer collimator which enables an integrated FOV of 0.0350sr for each instrument channel. The SDDs are equipped with $\approx 0.4 - 7.0$ keV and have an energy resolution of $E/\Delta E \approx 7$ near 0.7keV, thus providing low-resolution spectra over the full FOV (Kaaret et al., 2019; Miles, 2021). Thus, HaloSat can image Cygnus in one singular pointing, albeit at a lower spectroscopic resolution than tREXS (Miles et al., 2019; Miles, 2021).

HaloSat observed the Cygnus Loop as part of its mission to observe the diffuse emissions of the whole Milky Way hot halo. The pointings were taken at (RA, Dec) = (312.75, +30.67), or the approximate center of the Cygnus Loop (Miles, 2021). The data used for the HaloSat source model were taken from a ≈ 89 ks observation with two of the three instrument channels, namely detectors 38 and 54, defined in (Kaaret et al., 2019). Because of HaloSat’s designed purpose for the spectral imaging of ionized oxygen at 10^6 K and its ability to observe Cygnus in a single pointing, its observation of Cygnus will serve as an approximate substitute for a source model of the planned tREXS observation. By spectral fitting, the HaloSat data, more insight into the plasma evolution and conditions for Cygnus is also achievable. In this study, I present the results of a source model for Cygnus Loop using the HaloSat observation of Cygnus. The parameters of this source model will be run through an instrument model of tREXS created by Miles (2021), and return parameters for a predicted tREXS observation and result in the field. This can serve as a baseline of expectation for tREXS, and allow for some resolution to the discrepancies in the measurements for Cygnus’ plasma.

Chapter 2

Modeling of the Source Spectra: Methods & Results

2.1 The Uchida Model

Producing a representative model of the entire Cygnus Loop SNR requires a highly comprehensive model and analysis. A series of studies published by Uchida et al. (2008, 2009b,a) compiled a large array of observations from *XMM-Newton* and *Suzaku*. The Uchida source model was compiled between 2008 and 2009 and is one of the most comprehensive spectroscopic studies of the SNR. The spectral analysis was performed using ≈ 30 individual pointings. These pointings were then subdivided into 1000 sub-regions which were the sources of the extracted spectra used for the fitting and analysis. The individual pointings in relation to the Cygnus Loop SNR can be seen in Figure 2.1, whereas the pointing subregions can be seen in Figure 2.2

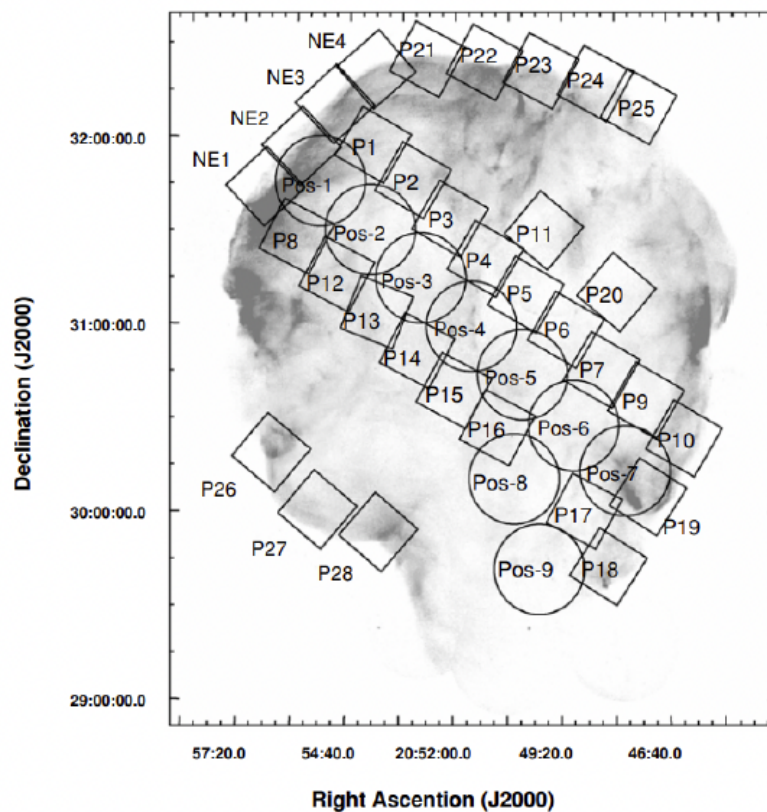


Figure 2.1: This Figure shows the *XMM-Newton* (circles) and *Suzaku* (squares) fields from Uchida et al. (2009b) overlaid on a ROSAT image of the Cygnus Loop supernova remnant from Levenson et al. (1999). Each FOV was further divided into a total of 1042 smaller regions from which spectra were extracted.

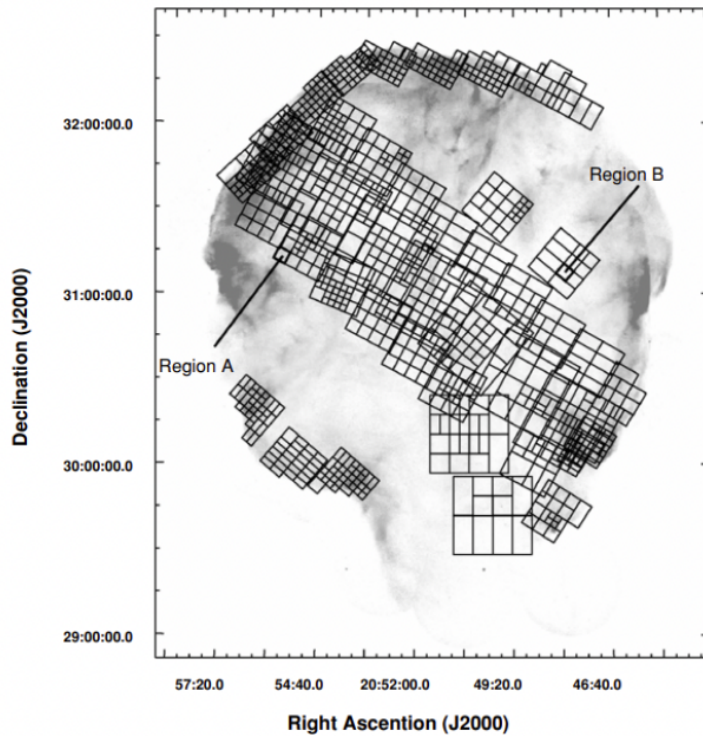


Figure 2.2: This Figure shows the specific sub-regions from which the Uchida et al. (2009b) extracted spectra for their model overlaid on a ROSAT image of the Cygnus Loop supernova remnant from Levenson et al. (1999).

The Uchida model found consistent results compared to other past comprehensive analyses of the Cygnus Loop SNR. Uchida et al. (2008, 2009a,b) found various regional disparities in temperature and plasma models. This shows that even with comprehensive sets of multi-pointing observations there is very little information regarding a global model for the Cygnus Loop SNR. For example, Uchida et al. (2008, 2009a) found that ejecta interacting with the ISM produces a two-temperature component NEI model for the interior of the Cygnus Loop SNR, whereas the cooling ejecta in the outer limbs can be fit with a single-temperature NEI model. To obtain a global representation of the remnant, a two-temperature NEI model was employed despite attempts to fit an NEI-CIE model combination. The global model found Table 2.1 shows the model parameters taken from Uchida et al. (2008, 2009a,b) which were utilized as a source model to build a predicted observation of Cygnus Loop SNR by tREXS. The predicted observation the Uchida source model produced will be compared against the novel HaloSat source model presented here.

Model Component	Value
$N_{\text{H}}[10^{22} \text{cm}^{-2}]$.0314
$kT_1[\text{KeV}]$	0.20
C	0.27
N	0.10
O	0.35
Ne	0.21
Mg	0.17
Si	0.34
S	0.17
Ar = Ca	0.20
Fe = Ni	0.20
$\tau[s \cdot \text{cm}^{-3}]$	1.2×10^{11}
Norm	1.0
$kT_2[\text{KeV}]$	0.50
C = N = O	0.19
Ne	0.28
Mg	0.16
Si = S	1.45
Ar = Ca	0.89
Fe = Ni	0.89
$\tau[s \cdot \text{cm}^{-3}]$	1.86×10^{11}
Norm	1.1

Table 2.1: Spectral fit parameters based on the findings in the Uchida et al. (2009b) derived model of the Cygnus Loop SNR. Elemental abundances are in terms of solar abundances.

2.2 The HaloSat Source Model

In more recent years, HaloSat’s large FOV provides an opportunity to fit source models to a single pointing global observation of the Cygnus Loop. This is in contrast with the Uchida source model from Section 2.1, which utilized multiple instruments and pointings. For this study, HaloSat’s observation of the entire remnant was used to generate models of the diffuse soft X-ray emission from Cygnus Loop, which are then passed through the tREXS instrument response code in Miles (2021) to generate a simulated observation.

Despite the limb being a model unto itself, because a more global representation is desired we will lump the limb into one of the two temperature regions and assume one of the two tem-

perature components of the model will cover it at full scale. The model chosen for this analysis was a two-temperature NEI model. The two-temperature NEI model will be built using XSPEC version 12.13.0 (Arnaud, 1996). The HaloSat source model results are shown in Table 2.2. Like the Uchida-based model, the source was modeled using absorbed NEI models from the *tbabs(vnei+vnei)* command in XSPEC. The absorption along the line of sight was accounted for by the Tuebingen-Boulder ISM absorption model for x-ray absorption along the line-of-sight, provided by the *tbabs* model in XSPEC (Arnaud, 1996). The contribution from the Hot X-Ray Background (HXRb) was taken into account using the *tbabs(pow)* model in XSPEC (Arnaud, 1996), or an absorbed power law with the same column density as the source model, and a photon index of 1.45 taken from the modeling of the CXB performed in Cappelluti et al. (2017). Liu et al. (2017) attempted to fit a Mewe-Gronenschild-Kaastra model for hot diffuse gas emission (*mekal* in XSPEC), an APEC model for collisionally-ionized diffuse gas (*apec* in XSPEC), and a Raymond-Smith model for hot diffuse gas emissions (*raymond* in XSPEC) (Liu et al., 2017; Arnaud, 1996). Liu et al. (2017) found that the Local Hot Bubble (LHB) emissions were best modeled by thermal ionization equilibrium. Using the findings of Liu et al. (2017) constrain the LHB, an APEC ionization equilibrium model was used (*apec* model in XSPEC) with solar abundances, a temperature of $kT \approx 0.097\text{keV}$ (Liu et al., 2017), and a redshift of $Z \approx 2.37 \times 10^{-8}$ as calculated using the Hubble Constant (Freedman and Madore, 2010) and the HXRb (Blair et al., 2005).

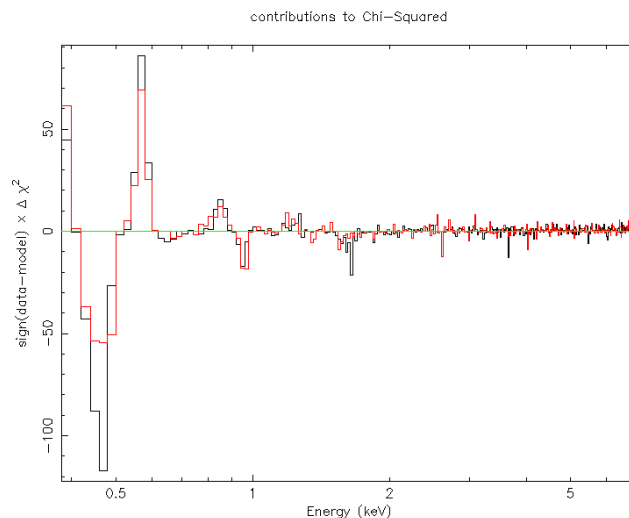


Figure 2.3: This figure shows the contribution to the chi-square goodness of fit with the 0.4 – 0.5keV range still present. Around the low energy range, the spectral fit contributes to worse goodness of fit. Figure 2.3 shows the data, fit, and reduced chi-square per energy for the model with these energy regimes removed.

The instrument component and noise were removed using the *arf* and *rmf* files also provided by Angelini et al. (2022). It should be noted that the *rmf* files for the instrument subtraction were different than that the *rmf* files for the spectral files. Thus, the instrument component was removed using a separate model from the model containing the source and HXRb-LHB model, which consisted of a two-component power law (*pow + pow* in XSPEC) with photon indexes and normalizations specific to HaloSats FOV and each detector provided by Angelini et al. (2022) and

Bluem et al. (2022). HaloSat is only capable of observing effectively within the 0.4–7.0keV range, thus, the model ignores spectra outside this range. It should be noted that for both models ignored spectra starting at 0.5keV instead due to heavy statistical uncertainty coming from the 0.4–0.5keV energy range (the 0.4 – 0.5keV range had already been omitted at this point). This would result in the model drastically depleting the abundances of other lighter elements, or depleting Carbon and Nitrogen, with either scenario resulting in inadequate abundances given the literature. When fitting, the heavier elements were left at Uchida abundance while the lighter elements such as C, N, and O were left to as free parameters. The temperatures, normalizations for the NEI models, the column densities in both the source and background model and the NEI model timescales were also set as free parameters.

Model Component	Value
$N_{\text{H}}[10^{22} \text{cm}^{-2}]$	0.129
Redshift	1.28×10^{-7}
χ^2_{ν}	1.502
$kT_1[\text{KeV}]$	0.27
C = N = O	0.23
Ne	0.64
Mg	0.74
Si = S	1.26
Ar = Ca	0.89
Fe	0.88
Ni	1.00
$\tau[s \cdot \text{cm}^{-3}]$	2.5×10^{10}
Norm	0.944
$kT_2[\text{KeV}]$	0.55
C = N = O	0.45
Ne	0.24
Mg	0.18
Si = S	0.34
Ar	0.17
Ca	0.20
Fe	0.20
Ni	0.20
$\tau[s \cdot \text{cm}^{-3}]$	1.302×10^{11}
Norm	0.447

Table 2.2: Spectral fit parameters for XSPEC using the HaloSat Spectra.

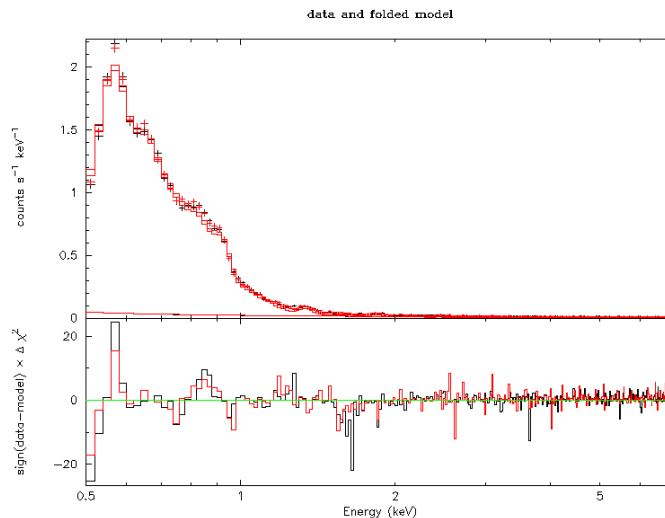


Figure 2.4: This figure displays a histogram of the data in black and red crosses, with the model fit in the solid red line. Below is the chi-square per energy, which has improved on the lower end with the removal of the 0-0.5KeV range of energies.

The initial model was comprised of an NEI model to represent the interior regions being heated by reverse shocks, and a CIE model (*vapex* in XSPEC) to represent the cooling ISM-ejecta plasma emissions. Fits with this NEI-CIE combination eventually produced a fit of $\chi^2_{\nu} \approx 1.93$, but provided physically unsupported abundances. The current two-component NEI model provided both a low fit ($\chi^2_{\nu} \approx 1.502$), as well as physically accurate abundances that agree well with the existing literature. The current source model suggests that the low-temperature reverse shocked interior component is younger than the hotter ISM-interacting ejecta component. This follows the expected evolution for an SNR, which undergoes a blast-wave expansion followed by a reverse shock through the ejecta upon contact with enough ISM (Spitzer, 1998; Chevalier, 1977). Thus, as the reverse shock propagates from the exterior ejecta to the interior of the SNR, the outer ejecta have longer to cool and are likely older plasmas Chevalier (1977); Spitzer (1998). This has been modeled before by past comprehensive multi-pointing observations of Cygnus such as Levenson et al. (1999); Tsunemi et al. (2007); Miyata et al. (2007); Uchida et al. (2008, 2009a). The calculated column density along the line of sight is slightly higher than what is expected for Cygnus in literature (Fesen et al., 1982; Weil et al., 2019), but falls within the established $10^{20} \lesssim N_{\text{H}} \lesssim 10^{21} \text{cm}^{-2}$ range. The suggested age for the low-temperature component is also lower than expected, however, it also falls within an acceptable range as established by past observations (Levenson et al., 1999; McEntaffer and Brantseg, 2011; Miyata et al., 2007; Uchida et al., 2008, 2009b,a). Figure 2.4 gives a statistical and graphical representation of the data. Figure 2.4 shows less uncertainty as the energies increase, with the most clustered around the smaller energy emissions and harder-to-resolve lines such as the O VII trio.

Chapter 3

The tREXS Instrument Model & Predicted Observation

3.1 The Instrument Model

The instrument model for tREXS was taken from the code and model created by Miles (2021). The instrument raytrace was built in the sequential order incoming photons would interact with each part of the optic. The raytrace is designed to take a source model of the emissions and return a predicted observed spectra for tREXS by simulating the passage of photons through the tREXS optic. Thus, the raytrace begins by simulating the passage of photons through the MBS'. The raytrace incorporates the dimensions of the entrance and exit slits, the spacing between each successive entrance and exit of the slit channels, the length of the module, the positions of each MBS, fabrication and alignment tolerances, and the desired FOV or total geometric area over which to populate the slit channels Miles (2021). Using these parameters, the raytrace model can predict the movement of photons of different wavelengths through the tREXS optic. The parameters for each MBS can be automatically read by the software using either an optimization code, from pre-existing specifications, or responses to a prompt to allow the user different parameter combinations. The following explanation of the raytrace will assume the tREXS-specific parameters (Miles, 2021).

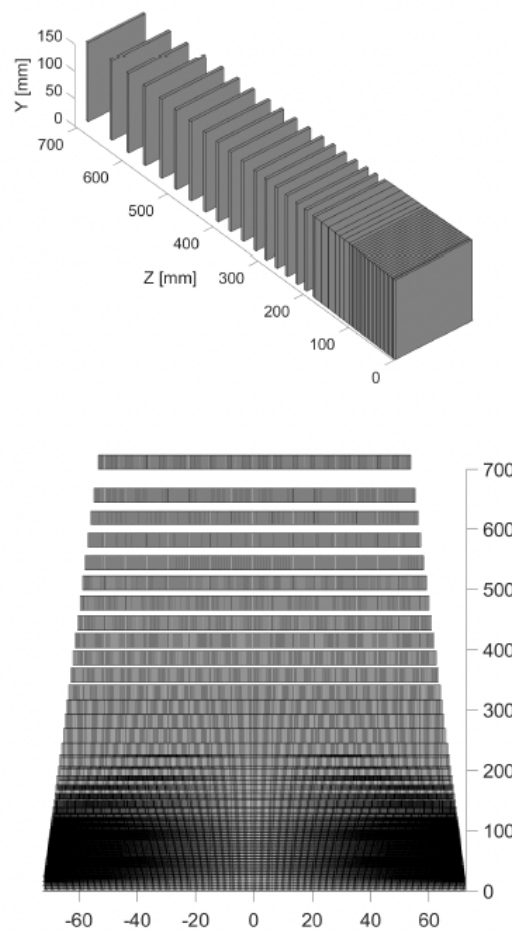


Figure 3.1: This image, taken from Miles (2021) displays an example of the instrument raytrace models rendering of the tREXS MBSs.

Using the initial parameter inputs, the full MBS models can be simulated. The simulation for the MBS modules is far more simplistic than that of a mirror instrument because the photons are passively focused. Thus, only the 3D geometry of the system and propagation of photons matter. To start, the convergence angles for the slits and slit spacing are at the position of each MBS plate. Following this, whole plates are constructed using the initial parameters, and the plates are built outward from the central slit. In the event there is no central slit (i.e. an even number per plate), the model starts with the two center slits and then builds outward. The successive slits are constructed in the model by iterating through the number of slits and adding slit positions accordingly (Miles, 2021).

The initial parameters are also used to determine the FOV of the MBSs and individual slit channels. The nature of the design allows for identical slit channels or plates to have identical FOVs, with the range of allowed incident angles will vary on each slit channel's position and convergence angle (Miles, 2021).

Following the construction of the MBS', the instrument model builds an idealized MBS plate series before adding on support frames and structure. The model then takes into account how the support structure affects the incoming photons. The frame support within the active collecting area is limited to only three crossbars, which are modeled as 1.1mm height, depth of 4mm, and width equal to a plate's aperture. The wires that act as the physical entity collectively responsible for the focusing of incoming photons are also modeled using their length, width, and depth (Miles, 2021).

The incoming photons are modeled as propagating along the z-axis of each MBS plate, with angular distribution determined by the tREXS field of view and the extent of the observed source. Their positions are updated based on their initial location and angular orientation. Photon positions are updated at each MBS plate and are checked against plate geometry to determine if they pass through onto the next or are absorbed by the wires, the crossbars, etc. Any photons whose positions intersect with wires, crossbars, or other physical barriers are considered occulted and removed. By propagating each incident photon as it passes through each plate, the MBS module results in the final shaped beam exiting the plate. Following this, the photons pass through the simulated gratings and determine the predicted spectra (Miles, 2021).

The grating array simulation is the next component of a full tREXS instrument simulation. As before with the MBS, the grating simulation starts with parameters such as the physical dimensions, spacing, orientation, groove density, and geometry of the gratings. From the initial parameters, the software can determine the full grating model using user-inputted values.

The creation of the simulated spectral gratings is similar to the method used for the MBS plates. The tREXS spectral gratings are stacked on top of one another in specific spacings. The instrument model software begins with one grating array and a 2D representation of the grating's cross-section in the direction of photon propagation and then builds outward. Once the physical model of the gratings is determined, the raytrace propagates the photons along the 50mm distance between the MBS module and the grating array. Each photon's passage is then separately analyzed to determine if it will become occulted by the substrate thickness or array support structure. Following an occultation check, each photon is propagated through the gratings until it intersects with either a grating surface, the bottom of the next grating substrate, or leaves the grating and becomes occulted by the grating module sidewalls (Miles, 2021).

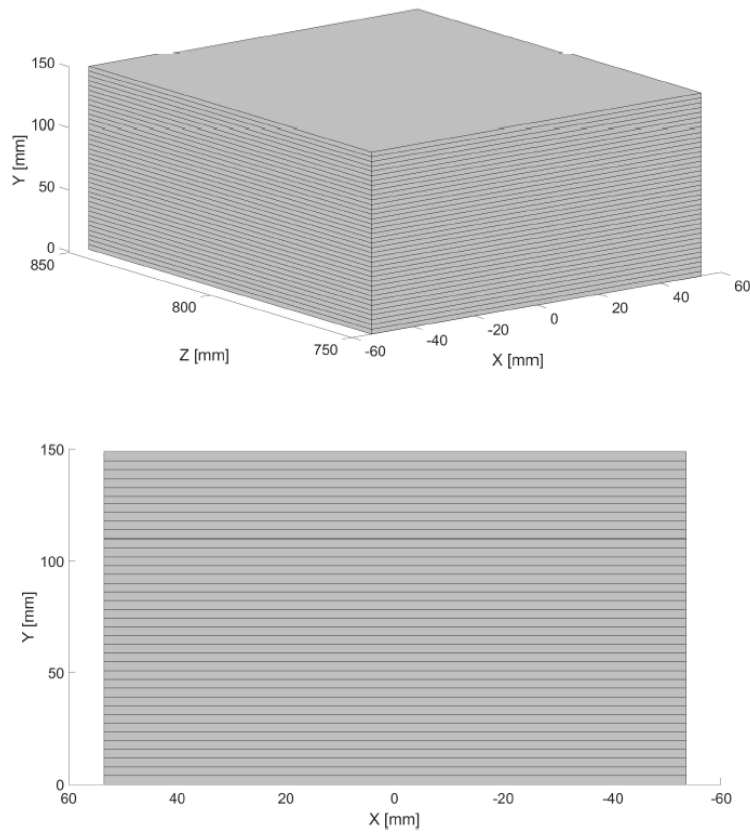


Figure 3.2: This image, taken from Miles (2021) displays the spectral grating dimensions and positions.

Photons that intersect a grating surface are assigned a specific grazing angle based on their directionality and the grating surface's orientation, and a diffraction angle is calculated using the groove density and the incident position for the photon and their wavelength. These photons are also transformed into grating coordinates and assigned values based on their directionality and grating diffraction. Grating efficiency is modeled using data from calibration tests of the flight gratings and an external grating efficiency software, such as PCGrate-SX (Miles, 2021).

The focal plane is the final component following the spectral gratings in the instrument raytrace. The raytrace propagates the photons down the remaining distance between the gratings and the detector electronics. Because of this, the model only needs to consider the distance traveled and the geometry of the detectors' active area, the detector quantum efficiency, and any support structure that could occult the photons. After being propagated across the distance between the gratings and detectors, the photons are checked for occultation by support structures. Photon trajectories and positions are checked to determine if they each have a valid path to the detector. Photons that pass through all components of the model are considered detected. These photons are then saved and put through a separate detector performance model for the CIS 113 detectors (Miles, 2021).

3.2 Prediction for the Observed Spectra of Cygnus Using tREXS

Using the described instrument model described in the previous section created by Miles (2021), the simulated source spectra from Section 2.2 is utilized as the source input component to the model. Figure 3.3 displays the resulting predicted spectra for tREXS generated using the HaloSat source model and Miles (2021)'s instrument model software.

The predicted source model displays two of the O VII triplets in prominence, with the resonance emission energy line being the most prominent and the forbidden line being the second most prominent. This is partly in due to the instrument model accounting for tREXS's capabilities, which cannot resolve the intercombination line within the O VII trio. The width of the bars in Figure 3.3, which indicate the quality of the resolution, is larger at higher wavelengths. This translates into higher resolution at lower energies, meaning that the desired lower energy emission lines are favored. This satisfies a main mission requirement for tREXS, which is to accurately capture the O VII and O VIII emissions in one high-resolution pointing.

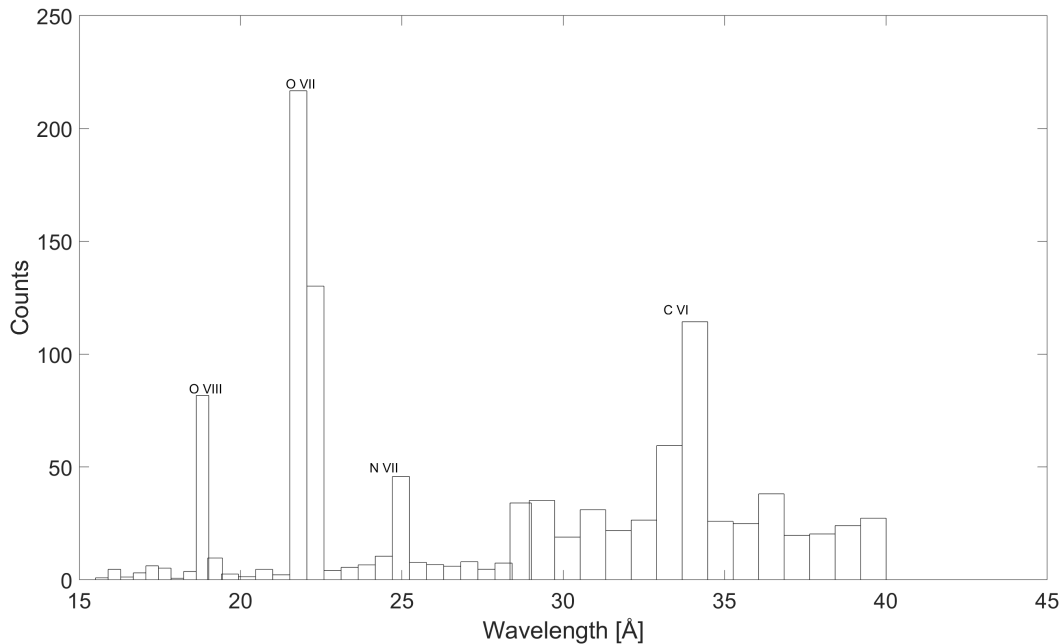


Figure 3.3: This figure generated by the instrument model displays the predicted observed spectra and line emissions by wavelength for tREXS. The width of the bars translates to the spectral resolving power at that wavelength, with width = $\Delta\lambda$. Emission lines that are the goal of the tREXS mission are indicated with text by the name. While two of the OVII lines can be shown, the third line is not displayed as this is beyond tREXS' resolving power.

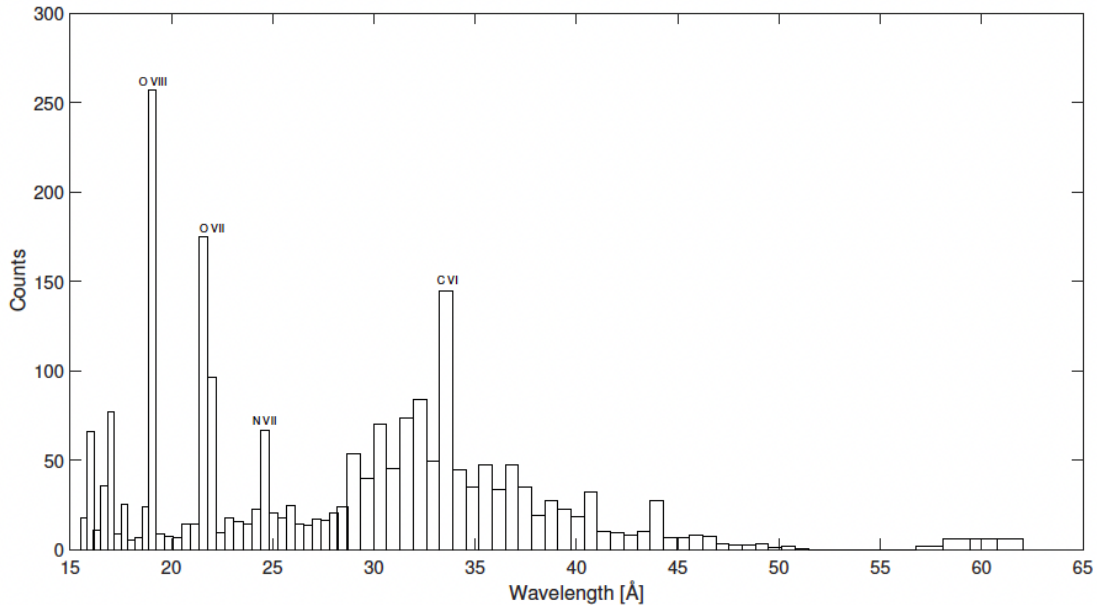


Figure 3.4: This figure from Miles (2021) generated by the instrument model using the Uchida-based source model displays the predicted observed spectra and line emissions by wavelength. In this predicted spectra, the O VIII line is dominant, with the O VII line as the second most intense, followed by the C VI line. As before, the width of the bars translates to the spectral resolving power at that wavelength, with width = $\Delta\lambda$.

Overall, the C VI is not the dominant emission line, with two of the three O VII trio lines being the most prominent. Specifically, we capture the resonance transition at $\lambda \approx 21.6\text{\AA}$ is the most prominent, followed by the forbidden line at $\lambda \approx 22.1\text{\AA}$ and the C VI line. Though, it is possible that due to the inability to resolve the forbidden O VII line at $\lambda \approx 21.8\text{\AA}$, the intercombination line's flux may be also factoring in the forbidden line flux as well. However, the Uchida-based predicted model had a much lower predicted ratio of O VIII to O VII intensity. Thus, if the predicted spectra for the HaloSat model hold, the predicted temperatures for the two temperature regions of Cygnus Loop SNR could be much higher. Moreover, this could suggest the presence of resonance, forbidden, and intercombination O VII lines at a global scale, which could denote the presence of some CIE behavior. This could also be the missing information necessary to apply a NEI-NEI-CIE model fit described in Uchida et al. (2019), which was previously inadequate due to the lack of O VII trio lines. Despite this, the Uchida models are still constrained by the potential error of multiple instruments and pointings, while HaloSat is limited by an energy resolution that cuts off at $\approx 0.4\text{keV}$ around where Cygnus Loops dominant feature, the highly ionized emissions of C, can be found.

The similarities between the predicted observation of a multi-pointing source model and a single-pointing observation also give credence to the physical observations gained from multi-pointing observations of Cygnus Loop SNR (Levenson et al., 1999; McEntaffer and Brantseg, 2011; Miyata et al., 2007; Uchida et al., 2008, 2009b,a; Uchida et al., 2019). For example, the low ratio in intensity between the O VII forbidden and resonance lines suggests lower temperatures at

the $\sim 0.1 - 0.5\text{keV}$ range and the usage of at least two NEI models as seen in Uchida et al. (2019). The presence of O at around 0.45 for the hotter component and 0.23 for the cooler component also validate this, as higher abundances would suggest higher intensities and thus temperatures for those regions and vice versa. This also suggests earlier claims by Uchida et al. (2019) of depletions in the C, N, and O abundances (between $\sim 0.2 - 0.4\odot$) are more valid, as we also see this in the model in Section 2.2 Uchida et al. (2008); Uchida et al. (2019); Kaaret et al. (2019). The O VII to O VIII intensity, also seen in Uchida et al. (2009a,b); Uchida et al. (2019), suggest that the remnant is not in a CIE phase at a large scale, but that the NEI-NEI model while adequate does not fully describe the high ratio in intensity between O VII and O VIII, suggesting that an NEI-NEI model with other sources of emission is probable.

Chapter 4

Discussion of Results & Concluding Remarks

4.1 Discussion

The Cygnus Loop SNR has been observed numerous times over the subsequent decades since its initial discovery (Levenson et al., 1999; McEntaffer and Brantseg, 2011; Miyata et al., 2007; Uchida et al., 2008, 2009b,a; Miles, 2021). Past observations of Cygnus have been done with and across various instruments, pointings, and years. This invariably leads to a wide array of errors due to Cygnus being studied mainly through the stacking of observations, each of which adds more error. As a result, there is no surprise that observations and models of the Cygnus Loop SNR's emissions and phenomena have yielded differing results. There are some agreed-upon characteristics, such as column density along the line of sight (Fesen et al., 1982), distance (Blair et al., 2005), and age (Tsunemi et al., 2007). More specifically, these have also led to the application of different best-fit models for different regions of Cygnus Loop SNR which can be hard to average into a general representation of the SNR (Tsunemi et al., 2007; Uchida et al., 2008; McEntaffer and Brantseg, 2011; Oakley et al., 2013; Miles, 2021). A single-pointing observation and spectra of the Cygnus Loop SNR thus become desirable as a potential solution to the localized picture of the Cygnus Loop (McEntaffer and Brantseg, 2011). Through a single-pointing observation, a general spectral model could be generated that represents the conditions for the Cygnus Loop holistically.

tREXS can achieve both the wide FOV and spectral energy resolution needed to image the desired emission features and capture the whole SNR in a single point. The tREXS design of a passive focusing mechanism that uses wired plates to shape incoming photons to the desired focus, combined with high-resolution modern spectral gratings allows for this. In light of the recent failure to detect photons in the initial launch of tREXS in September 2022, there becomes a need to model what the observed spectra might look like both to support existing literature and to provide future mission insights. The HaloSat data of Cygnus Loop SNR, though lower in resolution than tREXS, observed the whole SNR in a single pointing. The spectral source model generated from the HaloSat spectra of Cygnus produced a predicted spectrum from the tREXS instrument model, which takes emission source spectra and models how tREXS would view it. This predicted tREXS spectra yielded the potential for the desired O VII emission lines to be the most prominent spectral feature. The predicted model presented here shows that the O VII emission lines will be the dominant feature. This is in contrast with predictions that the O VIII emissions would be dominant (Uchida et al., 2008). The lack of C could be due to HaloSat's resolution dropping off around the high-energy C lines. The dominance of the O VII and O VIII lines however, presents the unique opportunity to validate Cygnus Loop SNR's age and evolutionary stage, as past observations in high resolution such as Vedder et al. (1986) failed to detect the key O VII forbidden lines used to characterize age and evolution.

The novel predicted spectra for tREXS presented herein was taken from a single HaloSat pointing and were compared to past tREXS predicted spectra by Miles (2021). The predicted spectra presented herein agree more in terms of dominant spectral features and flux with some of the most accurate and comprehensive multi-pointing models such as Uchida et al. (2008, 2009a,b); Uchida et al. (2019). The model presented here agreed with the Uchida based predicted tREXS observation in that O would dominate over C. However, they differ in that there is a large ratio between O VII and O VIII intensities. This does, however, agree with Uchida et al. (2019), which also predicts a similar O VII to O VIII ratio. The two predicted spectra were taken from NEI-NEI models, with a low and high-temperature component to measure the average plasma emissions from the

reverse-shocked interior and exterior ISM-interacting ejecta.

There is a considerable difference between the sources of error and methods employed to observe the Cygnus Loop SNR. The Uchida source model tREXS prediction has errors due to various instruments, multiple pointings, and other factors whereas HaloSat is constrained by its poor energy resolution at lower energies ($0 \lesssim kT \lesssim 0.4\text{keV}$). The source model presented here also cut off the energies $\lesssim 0.5\text{keV}$ and $\gtrsim 7.0\text{keV}$. This was due to the high error shown in Figures 2.3 and 2.4 in the lower energy ranges (Angelini et al., 2022; Bluem et al., 2022; Kaaret et al., 2019). Despite this, it can be validated that a two-temperature component NEI model best describes the Cygnus Loop SNR as past modeling attempts have shown (Levenson et al., 1999; Tsunemi et al., 2007; Uchida et al., 2008). The ages for the remnant, abundances (particularly the heavier elements), and the column density (despite being slightly higher than predicted) along the line of sight are generally in agreement with a few degrees of error. Future higher-resolution observations of Cygnus Loop SNR by tREXS could improve the lower energy uncertainties and provide better representations of the spectra.

4.2 Conclusion and Future Work

The Rockets for Extended-source X-Ray Spectroscopy have the potential to resolve conflicting models for the Cygnus Loop SNR, and provide one of the highest-resolution general models to date. The novel predicted tREXS observation using HaloSat data and presented here indicate that vital spectral features, such as the O lines and the C lines, could be resolvable at a general scale. Resolving these could provide the potential for better characterizations of the Cygnus Loop SNR's age, and evolutionary stage, and even provide better insight into the NEI-NEI vs NEI-CIE dispute. While a CIE model did not conform to elemental abundances unless extreme depletions or abundances were taken into account, it did provide a close fit. Moreover, these error-prone abundances were in the lower energies such as C, O, and N, indicating that the HaloSat resolution could be a reason why the model was unable to accommodate these elements. tREXS has the energy resolution to cover what HaloSat cannot, thus another modeling attempt using both an NEI-NEI and NEI-CIE model using real tREXS observed spectra may prove useful to resolving the plasma conditions. These observations could also be used to provide insight into the ongoing debate regarding the Cygnus Loop SNRs cavity explosion SN status as well.

Bibliography

- Angelini, L., Zajczyk, A., Kaaret, P., Bluem, J., and Ringuette, R. (2022). *HaloSat Analysis Guide, Version 1.5*. NASA Goddard Flight Center HEASARC, Greenbelt, Maryland.
- Arnaud, K. A. (1996). XSPEC: The First Ten Years. In Jacoby, G. H. and Barnes, J., editors, *Astronomical Data Analysis Software and Systems V*, volume 101 of *Astronomical Society of the Pacific Conference Series*, page 17.
- Blair, W. P., Sankrit, R., and Raymond, J. C. (2005). Hubble Space Telescope Imaging of the Primary Shock Front in the Cygnus Loop Supernova Remnant. , 129(5):2268–2280.
- Bluem, J. L., Kaaret, P., and Angelini, L. (2022). *HaloSat Background Analysis*. NASA Goddard Flight Center HEASARC, Greenbelt, Maryland.
- Bryans, P., Badnell, N. R., Gorczyca, T. W., Laming, J. M., Mitthumsiri, W., and Savin, D. W. (2006). Collisional Ionization Equilibrium for Optically Thin Plasmas. I. Updated Recombination Rate Coefficients for Bare through Sodium-like Ions. , 167(2):343–356.
- Cappelluti, N., Li, Y., Ricarte, A., Agarwal, B., Allevato, V., Tasnim Ananna, T., Ajello, M., Civano, F., Comastri, A., Elvis, M., Finoguenov, A., Gilli, R., Hasinger, G., Marchesi, S., Natarajan, P., Pacucci, F., Treister, E., and Urry, C. M. (2017). The Chandra COSMOS Legacy Survey: Energy Spectrum of the Cosmic X-Ray Background and Constraints on Undetected Populations. , 837(1):19.
- Chevalier, R. A. (1977). The interaction of supernovae with the interstellar medium. , 15:175–196.
- Ciotti, L. and D’Ercole, A. (1989). SNR expansion in a pre-existent cavity. , 215:347–359.
- Fesen, R. A., Blair, W. P., and Kirshner, R. P. (1982). Spectrophotometry of the Cygnus Loop. , 262:171–188.
- Freedman, W. L. and Madore, B. F. (2010). The hubble constant. *Annual Review of Astronomy and Astrophysics*, 48:673–710.
- Gorenstein, P., Harris, B., Gursky, H., Giacconi, R., Novick, R., and Bout, P. V. (1971). X-ray structure of the cygnus loop. *Science*, 172(3981):369–372.
- Grader, R., Hill, R., and Stoering, J. (1970). Soft x-rays from the cygnus loop. *The Astrophysical Journal*, 161:L45.

- Gronenschild, E. H. B. M. (1980). X-ray observations of the Cygnus Loop by ANS. , 85(1-2):66–76.
- Hester, J. J., Raymond, J. C., and Blair, W. P. (1994). The Balmer-dominated Northeast Limb of the Cygnus Loop Supernova Remnant. , 420:721.
- Kaaret, P., Zajczyk, A., LaRocca, D., Kirchner, D., Robison, W., Bluem, J., Fuelberth, W., Gulick, H., Haworth, J., McCurdy, R., et al. (2019). First results from halosat—a cubesat to study the hot galactic halo.
- Levenson, N. A., Graham, J. R., Aschenbach, B., Blair, W. P., Brinkmann, W., Busser, J. U., Egger, R., Fesen, R. A., Hester, J. J., Kahn, S. M., Klein, R. I., McKee, C. F., Petre, R., Pisarski, R., Raymond, J. C., and Snowden, S. L. (1997). The ROSAT HRI X-Ray Survey of the Cygnus Loop. , 484(1):304–312.
- Levenson, N. A., Graham, J. R., Keller, L. D., and Richter, M. J. (1998). Panoramic Views of the Cygnus Loop. , 118(2):541–561.
- Levenson, N. A., Graham, J. R., and Snowden, S. L. (1999). The Cygnus Loop: A Soft-shelled Supernova Remnant. , 526(2):874–880.
- Levenson, N. A., Graham, J. R., and Walters, J. L. (2002). Shell Shock and Cloud Shock: Results from Spatially Resolved X-Ray Spectroscopy with Chandra in the Cygnus Loop. , 576(2):798–805.
- Liu, W., Chiao, M., Collier, M. R., Cravens, T., Galeazzi, M., Koutroumpa, D., Kuntz, K. D., Lallement, R., Lepri, S. T., McCammon, D., Morgan, K., Porter, F. S., Snowden, S. L., Thomas, N. E., Uprety, Y., Ursino, E., and Walsh, B. M. (2017). The Structure of the Local Hot Bubble. , 834(1):33.
- McEntaffer, R. L. and Brantseg, T. (2011). Chandra Imaging and Spectroscopy of the Eastern XA Region of the Cygnus Loop Supernova Remnant. , 730(2):99.
- Miles, D. M. (2021). *A Reflection-Grating Spectrometer for Extended-Source Soft X-Ray Astronomy*. PhD thesis, State College PA.
- Miles, D. M., McEntaffer, R. M., Tutt, J. H., Anderson, T., Weiss, M., Baker, L., Weston, J., O’Meara, B., McCurdy, R. C., Myers, B., and Grisé, F. (2019). An introduction to the Rockets for Extended-source X-ray Spectroscopy. In Siegmund, O. H., editor, *UV, X-Ray, and Gamma-Ray Space Instrumentation for Astronomy XXI*, volume 11118 of *Society of Photo-Optical Instrumentation Engineers (SPIE) Conference Series*, page 111180B.
- Miyata, E., Katsuda, S., Tsunemi, H., Hughes, J. P., Kokubun, M., and Porter, F. S. (2007). Detection of Highly-Ionized Carbon and Nitrogen Emission Lines from the Cygnus Loop Supernova Remnant with the Suzaku Observatory. , 59:163–170.
- Oakley, P., McEntaffer, R., and Cash, W. (2013). Soft X-Ray Spectroscopy of the Cygnus Loop Supernova Remnant. , 766(1):51.

- Prokhorov, D. A. (2010). Non-equilibrium ionization states in galaxy clusters. , 509:A29.
- Sedov, L. I. (1993). *Similarity and dimensional methods in mechanics*. CRC press.
- Spitzer, L. (1998). *Physical Processes in the Interstellar Medium*.
- Tsunemi, H., Katsuda, S., Nemes, N., and Miller, E. D. (2007). The Plasma Structure of the Cygnus Loop from the Northeastern Rim to the Southwestern Rim. , 671(2):1717–1725.
- Tutt, J. H., Miles, D. M., McEntaffer, R., Anderson, T., Washington, D., Hillman, C., McCurdy, R., Zinski, N., O’Meara, B., and Baker, L. (2021). Developments of the focal plane camera for tREXS. In Siegmund, O. H., editor, *UV, X-Ray, and Gamma-Ray Space Instrumentation for Astronomy XXII*, volume 11821 of *Society of Photo-Optical Instrumentation Engineers (SPIE) Conference Series*, page 118210V.
- Tutt, J. H., Miles, D. M., McEntaffer, R. M., Anderson, T., Weiss, M., and O’Meara, B. C. (2019). The focal plane camera for tREXS. In Siegmund, O. H., editor, *UV, X-Ray, and Gamma-Ray Space Instrumentation for Astronomy XXI*, volume 11118 of *Society of Photo-Optical Instrumentation Engineers (SPIE) Conference Series*, page 111180C.
- Uchida, H., Katsuda, S., Tsunemi, H., Mori, K., Gu, L., Cumbee, R., Petre, R., and Tanaka, T. (2019). High forbidden-to-resonance line ratio of o vii discovered from the cygnus loop. *The Astrophysical Journal*, 871(2):234.
- Uchida, H., Tsunemi, H., Katsuda, S., and Kimura, M. (2008). The Plasma Structure of the Southwestern Region of the Cygnus Loop with the XMM-Newton Observatory. , 688(2):1102–1111.
- Uchida, H., Tsunemi, H., Katsuda, S., Kimura, M., and Kosugi, H. (2009a). Ejecta Distributions of Heavy Elements in the Cygnus Loop. , 61:301.
- Uchida, H., Tsunemi, H., Katsuda, S., Kimura, M., Kosugi, H., and Takahashi, H. (2009b). Line-of-Sight Shell Structure of the Cygnus Loop. , 705(2):1152–1159.
- Vedder, P. W., Canizares, C. R., Markert, T. H., and Pradhan, A. K. (1986). High-Resolution X-Ray Spectroscopic Evidence on Nonequilibrium Conditions in the Cygnus Loop. , 307:269.
- Weil, K., Fesen, R. A., Blair, W. P., and Raymond, J. C. (2019). The Cygnus Loop’s Distance, Properties & Environment Driven Morphology. In *Supernova Remnants: An Odyssey in Space after Stellar Death II*, page 63.
- Zhou, X., Bocchino, F., Miceli, M., Orlando, S., and Chen, Y. (2010). The origin of the X-ray-emitting plasma in the eastern edge of the Cygnus Loop. , 406(1):223–229.

Vincent A. Smedile

Curriculum Vitae

Permanent Address: 4726 198 Street, Flushing NY 11358
 Current Address: 600 E Pollock Rd 1401C Nittany Apts. 14, State College PA 16801
 vas5312@psu.edu +1 917 444-0416

EDUCATION

The Pennsylvania State University	University Park, USA
B.S. Astronomy & Astrophysics	May 2023 (Expected)
B.S. Political Science	May 2023 (Expected)
<i>Schreyer Honors Scholar & Paterno Fellow</i>	

RESEARCH EXPERIENCE

Penn State University – University Park, PA	
<i>Undergraduate Research Assistant with The McEntaffer Group</i>	March 2021 – Present

TECHNICAL SKILLS

Python, MATLAB, R (for statistical purposes), Programmable Logic Controllers (PLCs), Jupyter Notebooks, Office, Windows, Unix, LaTeX, science website management, science outreach, general lab skills, chemical storage procedures, teamwork, analytical problem-solving, and cleanroom procedures

PUBLICATIONS AND PROJECTS

1. Sofia Z. Sheikh, Grayce Brown, Brenda Jones, Mariah G. MacDonald, Jackson R. MacTaggart, Thomas Nguyen, Grace Rosario, **Vincent A. Smedile**, Adam T. Stone, and Shengdi You A Compilation of Pulse Widths and Their Associated Observing Parameters for All Known Nulling Pulsars *Research Notes of The American Astronomical Society* 5 (128) 5 vol2020 <https://iopscience.iop.org/article/10.3847/2515-5172/ac053f/meta>
2. **The Rockets for Extended-source X-Ray Spectroscopy (tREXS)**
The McEntaffer Group at Penn State March 2021 – September 2022
3. **The Off-plane Grating Rocket Experiment (OGRE)**
The McEntaffer Group at Penn State September 2022 – Present

4. **Vincent A. Smedile** “Soft X-Ray Source Modeling of the Cygnus Loop Predicted Observation for the Rocket for Extended-source X-Ray Spectroscopy” (Honors Thesis), *The Pennsylvania State University Schreyer Honors College, April 2022*

AWARDS & HONORS

Schreyer Academic Excellence Scholarship
Homer F. Braddock Scholarship Recipient
Paterno Fellows Program

August 2019-Present
August 2019-Present
January 2022-Present